Journal of Materials Chemistry A

Modulating the cross-plane thermal conductivity of graphite by $MnCl_2$ and $FeCl_3$ co-intercalation

Journal:	*Journal of Materials Chemistry A*
Manuscript ID	TA-ART-05-2024-003644.R1
Article Type:	Paper
Date Submitted by the Author:	25-Jul-2024

Complete List of Authors:	Chandra, Harsh; University of Tokyo Sasano, Shun; The University of Tokyo, Xu, Bin; University of Tokyo, Ishikawa, Ryo; University of Tokyo Noda, Suguru; Waseda University, Department of Applied Chemistry Shibata, Naoya; The University of Tokyo, Institute of Engineering Innovation Shiomi, Junichiro; University of Tokyo,

ARTICLE

Modulating the cross-plane thermal conductivity of graphite by $MnCl_2$ and $FeCl_3$ co-intercalation

Received 00th January 20xx,
Accepted 00th January 20xx

DOI: 10.1039/x0xx00000x

Harsh Chandra[a], Shun Sasano[b], Bin Xu[a,b], Ryo Ishikawa[b], Suguru Noda[c], Naoya Shibata[b], Junichiro Shiomi[a,b],†

Understanding thermal transport in graphite intercalation compounds can facilitate the development of novel methods to design materials with tunable thermal conductivities. This study reports the effective modulation of the cross-plane lattice thermal conductivity of graphite by co-intercalation with $MnCl_2$ and $FeCl_3$. Scanning transmission electron microscopy and electron energy-loss spectroscopy indicated that the predominant phase in the system corresponded to stage-3 structural ordering with the preferential intercalation of $MnCl_2$, despite the significantly higher amount of $FeCl_3$used for synthesis (300 times) compared with that of $MnCl_2$, indicating an extremely high intercalation selectivity of $MnCl_2$ in the adopted process-parameter window. Time-domain thermoreflectance measurements demonstrate that intercalation reduced the thermal conductivity of graphite by up to six times at 298 K and 10 times at lower temperatures. The significant tunability of thermal conductivity was obtained for a wide range of thicknesses, varying from 30 nm to 1.5 µm. A semi-empirical Debye-Callaway model that considered the effect of intercalation in an interfacial-scattering fashion explains the temperature dependence of the thermal conductivity of graphite on intercalation. It revealed that intercalation suppressed the effective phonon-transport length of the system by two orders of magnitude. This study could guide future studies on the fabrication of novel materials with excellent cross-plane thermal-conductivity tunability through intercalation.

Keywords: *graphite intercalation compound, co-intercalation, thermal conductivity, phonon scattering, transmission electron microscope*

Introduction

Over the last few decades, the science and engineering of the thermal transport of nanostructured crystalline materials have advanced significantly. Phenomena that govern heat conduction in materials across various lengths have been identified, such as non-Fourier quasi-ballistic transport[1, 2], anomalous low-dimensional transport[3, 4], coherent transport[5], and hydrodynamic transport[6]. Moreover, several studies on thermal transport in nanostructured materials have investigated low-thermal-conductivity thermoelectrics, thermal insulators, and nanostructures with lengths that are smaller than the phonon mean free path (p-MFP)[1, 7, 8]. Although the p-MFP of a system depends upon the phonon mode (frequency, wavevector, and polarization) and is distributed over a wide range of lengths (from nanometers to sub-micrometers), the general rule of thumb is that a smaller structural length is associated with a larger reduction in thermal conductivity. In this regard, superlattices with single-digit nanometer length scales have been widely investigated and have been shown to significantly impede thermal transport in the cross-plane direction (the direction that is perpendicular to the interface), both in terms of particle scattering and the wave interference of phonons[9-12].

Van der Waals (vdW) heterostructures, which comprise an array of stacked 2D crystals and show a sub-nanometer structural length, are representative examples of such superlattice structures[11, 13-15]. These heterostructures can contain a wide variety of 2D materials, including graphene[16-18], transition metal dichalcogenides[19, 20], and MXenes[21-30]. Studies on vdW heterostructures with structural contrasts in mass, geometry, and rotational angle indicate that these systems exhibit an extremely low cross-plane thermal conductivity[31-35].

An extended form of heterostructures with a large structural contrast is the intercalation compounds, where guest ions or molecules are inserted into the vdW interplanar gaps of the host 2D layered materials. The insertion of large ions and molecules enhances the mass contrast in the system, increases the interplanar gaps, and weakens the interlayer interaction, thereby reducing the thermal conductivity of the system. Additionally, the reversibility of intercalation enables thermal conductivity switching. Intercalation compounds comprising various layered materials and Li exhibit significant thermal conductivity tunability. On Li intercalation, black phosphorus exhibits a five-fold increase in thermal conductivity[36], while TiO_2 and V_2O_5 exhibit ~20% thermal-conductivity tunability[37] and MoS_2 shows an approximately five-fold thermal-conductivity

[a] *Department of Mechanical Engineering, The University of Tokyo, 7-3-1 Hongo, Bunkyo, Tokyo 113-8656, Japan*
[b] *Institute of Engineering Innovation, The University of Tokyo, 7-3-1 Hongo, Bunkyo, Tokyo 113-0032, Japan*
[c] *Department of Applied Chemistry, Waseda University, 3-4-1 Okubo, Shinjuku-ku, Tokyo 169-8555, Japan*
† shiomi@photon.t.u-tokyo.ac.jp
Supplementary Information available: [details of any supplementary information available should be included here]. See DOI: 10.1039/x0xx00000x

tunability[38]. Upon electrochemically oxygenating and hydrogenating $SrCoO_{2.5}$, the thermal conductivity of the system reversibly increases and decreases by 2.5 and four times, respectively[39]. Moreover, the thermal conductivity of Bi_2Se_3 and TiS_2 nanoribbons undergo significant reduction upon Cu and organic-ion intercalation, respectively[40-42].

Among the different types of intercalated compounds reported to date, graphite intercalation compounds (GICs) have been extensively investigated. GICs, which comprise graphite layers intercalated with various guest molecules or ions, show a series of structural configurations consisting of distinct alternating layers labeled stage-*n*, where *n* represents the number of graphite layers sandwiched between two consecutive layers of the guest intercalant. The phonon density of states (PDOS) in such systems can be significantly modulated by varying the effective mass and force constant between the graphite layers[43]. For instance, heavier intercalants (such as $FeCl_3$) and smaller atoms (such as Li and K) soften and stiffen certain phonon modes, respectively, causing a redshift[44] and blueshift[45] in the PDOS, respectively. Consequently, the c-axis thermal conductivity of stage-*5* K-GICs and stage-*2* $FeCl_3$-GICs with a red-shifted PDOS is significantly reduced to 1.25 and 1.5 W/m·K, respectively; additionally, molecular dynamics simulations indicate an initial reduction in the thermal conductivity of LiC_{18} with a blue-shifted PDOS to 1.3 W/m·K. To the best of our knowledge, very few studies have explored the tunability of the cross-plane thermal conductivity in GICs theoretically and experimentally. Furthermore, to date, there are no reports on the thickness or temperature dependence of the thermal conductivities of GICs.

In the course of enhancing the tunability of the GIC thermal conductivity, one interesting feature worth exploring is the co-intercalation, which involves the intercalation of more than one element into graphite to form co-intercalated GICs (co-GICs). In general, co-GICs[46, 47] comprise layered structures containing two distinct entities, atoms, ions, or molecules that are intercalated into the galleries between the host graphitic layers. The intercalated species can coexist within the same space or remain separated in different (not necessarily contiguous) galleries. Consequently, co-GICs exhibit a broad range of intra- and inter-planar structural configurations. A diverse array of co-GICs can be synthesized by combining two acids or an acid with an inorganic salt[48-50]. Typically, co-GICs contain large intercalant molecules such as $AlCl_3$-$FeCl_3$-GICs[51, 52], GIC-$(FeCl_3)_x$-$(CHCl_3)_y$, GIC-$(FeCl_3)_x$-$(CH_3NO_2)_y$, and GIC-$(FeCl_3)_x$-$(H_2O)_y$[53-55]. To the best of our knowledge, the thermal conductivity of co-GICs remains largely unexplored to date.

This study aims to understand the tunability of the thermal conductivity of GICs by investigating the thickness and temperature dependence of the thermal conductivity of co-GICs synthesized by co-intercalating graphite with two large molecules ($MnCl_2$ and $FeCl_3$). Co-intercalation reduced the thermal conductivity of graphite by nearly an order of magnitude. Several experimental techniques were used to investigate the temperature and sample-thickness dependence of the thermal conductivity. Furthermore, relative contributions of different possible phonon-scattering mechanisms, such as intrinsic phonon-phonon scattering, boundary scattering, and intercalant-induced scattering, to the thermal conductivity of the system were explored by employing a semi-empirical particle scattering based theoretical Debye-Callaway model[56]. Intercalant-induced scattering significantly shortened the effective p-MFP of the GIC, thereby reducing its thermal conductivity.

Materials and Methods

Sample preparation

First, graphite flakes with different thicknesses (30 nm to 1.1 µm) were exfoliated on a pretreated and cleaned Si wafer by micromechanical cleavage using a scotch tape[57]. Subsequently, co-GICs were synthesized by the one-zone vapor transport method shown in Figure 1(a). Graphite flakes were mounted on top of a quartz plate along with the intercalant (iron(III) chloride, anhydrous, 98%) with a boiling point of 316 °C and heated to 400 °C inside a quartz-tube reactor furnace at 1 atm argon pressure for 4 h. Film thickness is measured by AC tapping AFM mode with scan rate of 0.75 Hz.

Quantitative detection of Mn concentration

$FeCl_3$ powder, high-purity deionized water, and an acid that functioned as a digestion reagent (nitric acid; HNO_3) were used to detect traces of Mn in $FeCl_3$ powder using ICP–OES (Agilent5100 shown in Figure S2.1). The sample for analysis was prepared by dissolving $FeCl_3$ (100 mg) in nitric acid (10 mL), cooling the solution to room temperature, and diluting to 100 mL with ultrahigh-purity water. A specific wavelength was selected to prevent interference between Fe and Mn, as the concentration of Fe was expected to be 100 times greater than that of Mn. For details see Supporting Information Section S2.

Microstructure analysis

An electron-transparent thin specimen for S/TEM analysis was fabricated by a focused ion-beam system (FIB; Helios 5 UX, Thermo Fisher Scientific). To avoid significant ion-beam damage in the FIB process, an Au protective thin film was first deposited on the graphite sample followed by carbon deposition (S3.1(a)). A small portion of the sample was cut and lifted onto a copper grid, and then thinned by Ga ions accelerated at 2 kV in the final stage. The bright-field TEM images shown in Figure S3.1(a-b) and SAED patterns shown in Figure 2(b,c) were recorded by a JEOL 2010HC instrument operated at 200 kV. The results confirmed the formation of intercalated graphite with a thickness of 60 nm; the SAED patterns of the compounds contained characteristic diffraction spots. ADF–STEM images and electron energy-loss spectra (Quantum, Gatan Inc.) were acquired using a JEOL ARM300CF instrument equipped with a Delta-type corrector and cold-field-emission gun operated at 300 kV. The convergence and collection semi-angles were 30 and 90–200 mrad, respectively. To improve the signal-to-noise ratio, a sequential averaging method was used for the ADF–STEM images.[58] The oxidation state of Mn was estimated by the peak position and the integrated intensity ratio between Mn-L_3 and Mn-L_2 edges, as shown in Figure S3.2(b), (c). By referring the previous report of EELS spectrum in Figure S3.2(a), the oxidation state was determined to be 2+. Furthermore, the relative elemental composition of the system was estimated to be C:Cl:Mn:Fe = 77:14.6:7.0:0.97, using the ratio of integrated intensities of C-*K*, Cl-$L_{2,3}$, Mn-$L_{2,3}$, Fe-$L_{2,3}$ and their scattering cross-sections for core-loss EELS.

The presence of Mn in the 2+ oxidation state indicates that Mn existed in the form of chloride $MnCl_2$ in the powder. Further analyses are necessary to elucidate the underlying mechanism governing the selective intercalation of Mn over Fe at the current experimental parameter window in the system under investigation. For details, see Supporting Information Section S3.

Stage identification and spatial distribution

Raman spectroscopy measurements (inVia, Renishaw) was performed using a 633-nm laser and a wavenumber resolution of ~1 cm^{-1}. The silicon substrate and its characteristic peak at 520 cm^{-1} was used for fine calibration. The G-peak splitting and softening before and after intercalation were evaluated, and mapping was done to characterize and determine the stage homogeneity. For details see Supporting Information Section S4.

Mapping elemental chemical composition

SEM (JEOL JSM-6610LV) and EDX (JEOL JED-2300) were used for the elemental chemical-composition mapping of the intercalant powder, host graphite, and co-GIC, as shown in Figure S6.1(a) and Figure S6.2(a), at 20.0 kV 15.9 mm × 45.0 k SE(U) depicting atomic percentages of constituent elements. Experimental data indicated that co-GIC contained a higher concentration of Mn than Fe, possibly owing to the experimental conditions, i.e., the temperature and pressure, which allowed Mn to intercalate more readily than Fe. The origin of Mn in the co-GICs were confirmed by the EDX of the sample powders, as shown in Figure S6.2, which indicated trace quantities of Mn. For further details, see Supporting Information Section S5.

Theoretical modelling to identify the scattering mechanism

The Debye Callaway modelling of phonon frequency and temperature dependent thermal conductivity based on key underlying particle scattering events and their individual relaxation rate is employed to fit temperature variation of thermal conductivity experimental data. The theoretical expression for cross-plane (c-axis) thermal conductivity (κ) is given by

$$\kappa = \kappa_{debye} + \kappa_{callaway} = \frac{k_B{}^4 T^3}{2\pi^2 v \hbar^3} \int_0^{\frac{\theta_D}{T}} \frac{\tau_C x^4 e^x}{(e^x-1)^2}\, dx + \frac{k_B{}^4 T^3}{2\pi^2 v \hbar^3} \frac{\left(\int_0^{\frac{\theta_D}{T}} \frac{\tau_C x^4 e^x}{\tau_N (e^x-1)^2}\, dx\right)^2}{\int_0^{\frac{\theta_D}{T}} \frac{\tau_C x^4 e^x}{\tau_N \tau_R (e^x-1)^2}\, dx}$$

Key phonon-scattering phenomena, namely, Umklapp scattering, impurity scattering, boundary scattering from the edges of sample before and after intercalation, and intercalation scattering originating from the foreign-atom guest layers with the scattering rates τ_U^{-1}, τ_{Imp}^{-1}, τ_B^{-1}, and τ_{Intc}^{-1}, respectively, considered in this study are quantified in detail in Supporting Information Section S6.1.

Thermal conductivity measurement

TDTR was measured using a femtosecond laser with a pulse width of 140 fs and a repetition frequency of 80 MHz. The TDTR method is well documented in the literature[59, 60]. A pump pulse (wavelength of 400 nm) was used to heat a 95-nm-thick aluminum transducer deposited on the sample surface, and a probe pulse (wavelength of 800 nm) was used to measure the temperature changes. The laser-spot sizes of the pump and probe beam showed radii of 7–30 µm and 5–15 µm, respectively, for different parameters of interest. Modulation frequencies of 1.111 and 11.05 MHz were used for lock-in detection to enhance the detection sensitivity of crossplane thermal conductivity. Low-temperature measurements were conducted in a vacuum cryostat using liquid nitrogen. The solution of the standard heat-conduction model was fitted to the temperature decay profile with a delay time > 200 ps to quantitatively extract the thermal conductivity along the c axis of the sample in the temperature range of 78–298 K. Prior to thermal-conductivity measurements, a sensitivity analysis was used to identify the sources of uncertainties that could affect the precision of the data. Longitudinal velocities for the materials were extracted from the TDTR fits for modeling. The velocity of sound propagation was calculated from the thickness of the material and the time required for the acoustic wave to travel through the material. Time-of-flight information, which corresponds to the time required for the acoustic wave to traverse a film, can be extracted from picosecond acoustic echoes in the reflectivity data of systems. By combining this information with the film thickness (which is known), the velocity of sound propagation was determined using the above-mentioned formula. For details, Supporting Information Section S1.

Results and Discussion

First, graphite flakes with thicknesses in the range of 30 nm to 1.1 µm were exfoliated on a pretreated and cleaned Si wafer by micromechanical cleavage using a scotch tape. This enabled synthesis of varying thicknesses of graphite flakes from 30 nm to 1.1 µm. Subsequently, GICs were synthesized using the one-zone vapor transport method shown in Figure 1(a); graphite flakes were mounted on a quartz plate with the intercalant powder (iron (III) chloride, anhydrous, 98%, Alfa Aeser) with a boiling point of 316 °C and heated to 400 °C inside a quartz-tube reactor under an argon pressure of 1 atm for 4 h (See Materials and Methods).

Figure 1(b), (d), and (e) show the atomic force microscopy (AFM) and Raman spectroscopy scans of a 30-nm-thick graphite flake before and after intercalation. Upon intercalation, the thickness of graphite along the c-axis increases from 30 to ~45 nm. This structural-configuration change owing to the diffusion of guest atoms into the sub-nanometer vdW interlayer spacings of graphite modulates the intrinsic properties of the system by charge modification[43, 61, 62]. Figure 1(c) and (e) indicate a substantial change in the Raman peaks of graphite on intercalation. These data were fitted to a Lorentzian curve. The characteristic G peak of graphite at 1580 cm^{-1} underwent significant splitting into two distinct

degenerate peaks (P1 and P2), which were blue-shifted by ~5 and 25 cm^{-1}, respectively, from the original G peak. The experimentally observed peak splitting and structural stiffening upon intercalation are consistent with the literature[44, 63]. The modified graphite structural configuration predominantly exhibited *stage-3* lattice structural ordering, with three layers of graphite sandwiched between two consecutive guest-atom layers. Spatial Raman mapping

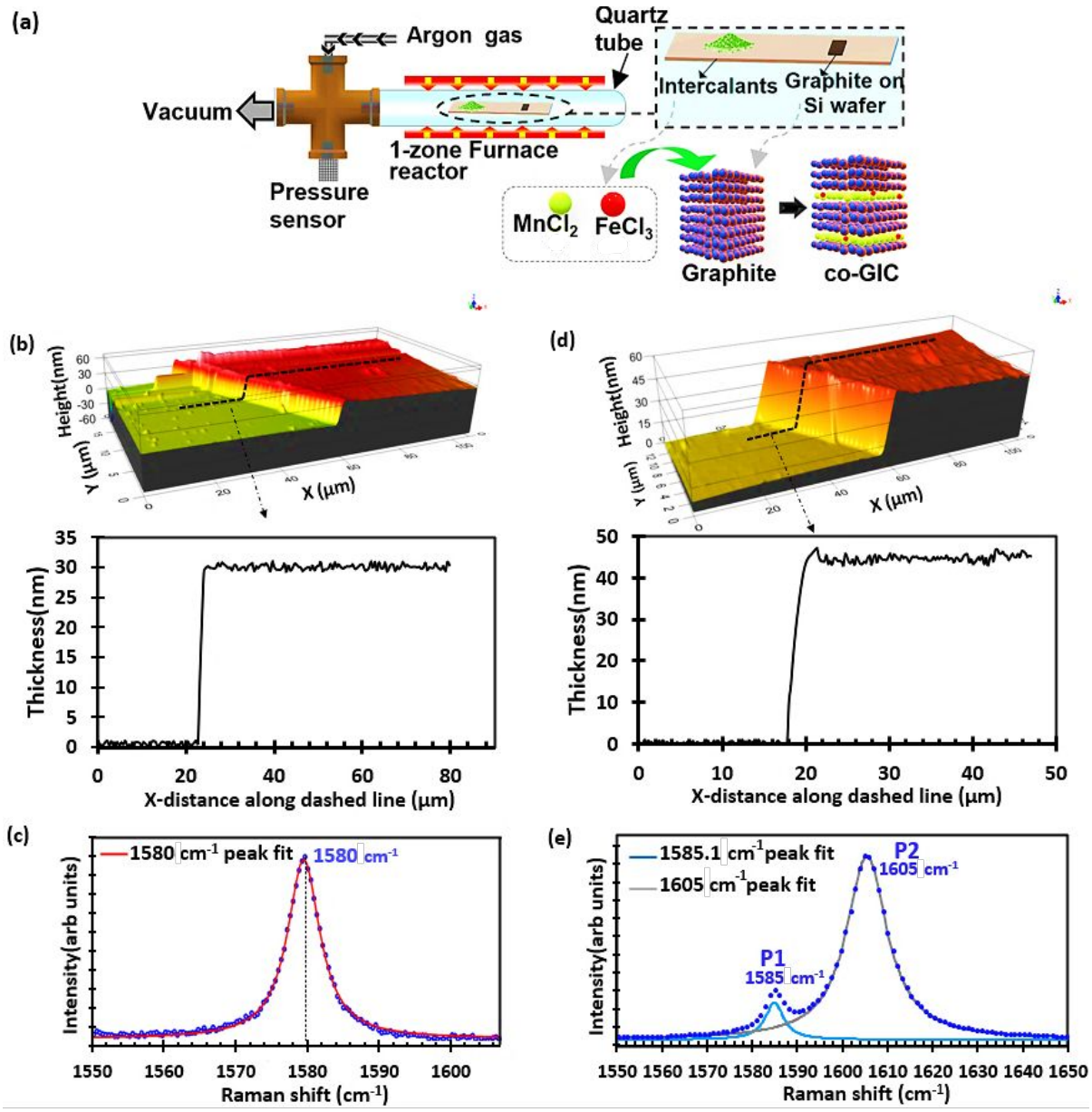

Figure 1: (a) Experimental setup of GIC synthesis. AFM thickness scans of 30-nm thick pristine graphite (b) pre and (d) post intercalation. The black dashed line indicates the analysis line. The step-height result indicates flake expansion from 30 to 45 nm. Raman spectra of 30-nm thick pristine graphite (c) pre and (d) post intercalation. The characteristic peak of graphite at 1580 cm^{-1} is split into two degenerate peaks (P1 and P2) at 1585 and 1605 cm^{-1}, respectively.

on a 20 µm × 20 µm region before and after intercalation confirmed the homogeneous and uniform distribution of the stage-*3* lattice structural ordering over a wide area (See Supplementary Information Section S4).

To directly observe the staging phenomenon, the morphology and crystallographic orientation of the GIC samples were investigated using selected-area electron diffraction (SAED)[64, 65] and annular dark-field scanning transmission electron microscopy (ADF–STEM)[66] as shown in Figure 2(a-c). In Figure 2(a), the SAED analysis of the diffraction spots in reciprocal space confirms the prevalence of stage-*3* lattice ordering. The image contains bright spots originating from intercalant-layer reflection. The reflection spots corresponding to the characteristic hexagonal (0002) lattice plane of graphite[65], which are positioned at 2.94 nm^{-1} apart in reciprocal space, *i.e.*, a separation of 0.34 nm in real space. A typical SAED pattern of a mixed-stage structure with a dominant stage-*3* phase exhibits four SAED spots corresponding to stage-*3* lattice ordering between the center and the (0002) lattice plane of graphite. The stage-*3* diffraction pattern shows streaks along the [0001] direction but

contains several diffuse spots, as indicated by white arrowheads in Figure 2(a), because of the long-range ordering of stage-*3*. Therefore, the analyzed sample consisted predominantly of a stage-*3* lattice phase along with small amounts of other mixed stages. As expected from SAED analysis, the ADF–STEM image in Figure 2(b) indicates the staging phenomena in the intercalant layers as bright horizontal lines stacked within layers of graphite and dark horizontal lines. The bright layers span the entire image horizontally, indicating uniform and complete intercalation by the guest molecules. The magnified ADF–STEM image in Figure 2(c) quantitively identifies an expansion in the interplanar vdW gaps of graphite from 3.42 ± 0.25 to 9.36 ± 0.16 Å on intercalation, with an intercalant repeat distance of 15.93 ± 0.15 Å. The histogram analysis of the stage distribution in Figure 2(d) confirms the predominance of the stage-*3* phase, consistent with the results of Raman spectroscopy.

The elemental composition and spatial distribution of the intercalated sample were qualitatively analyzed by electron energy-loss spectroscopy (EELS) (Figure 2(e–k)). Due to resource-intensive nature of TEM-EELS measurement, we could only measure one sample, but the measurement was performed on a GIC sample that was synthesized in same batch as the other three GIC samples, and thus, the results in Figure 2 are representative of the entire batch, ensuring that the variations in thermal conductivity observed among the samples are due to their thickness differences rather than variations in elemental concentration. Note that although SEM-EDX can be performed for multiple samples, quantifying graphite/intercalant ratio is difficult due to carbon contamination induced during the SEM process, and SEM-EDX was used primarily to identify the Fe/Mn ratio as shown in Figure S5.2 in Supplementary Information S5. The EEL spectra contained absorption edges corresponding to the expected elements, such as C, Cl, and Fe, at their characteristic energy levels. Interestingly, although the powder used for sample preparation contained 98 wt% of $FeCl_3$, the spectrum of the sample contained a sharp absorption-edges corresponding to Mn, which was significantly more intense than that of Fe. Further analysis of the intercalant guest-element distribution in the sample by EELS spatial mapping confirmed the preferential and predominant intercalation of Mn in the GIC with only traces of Fe.

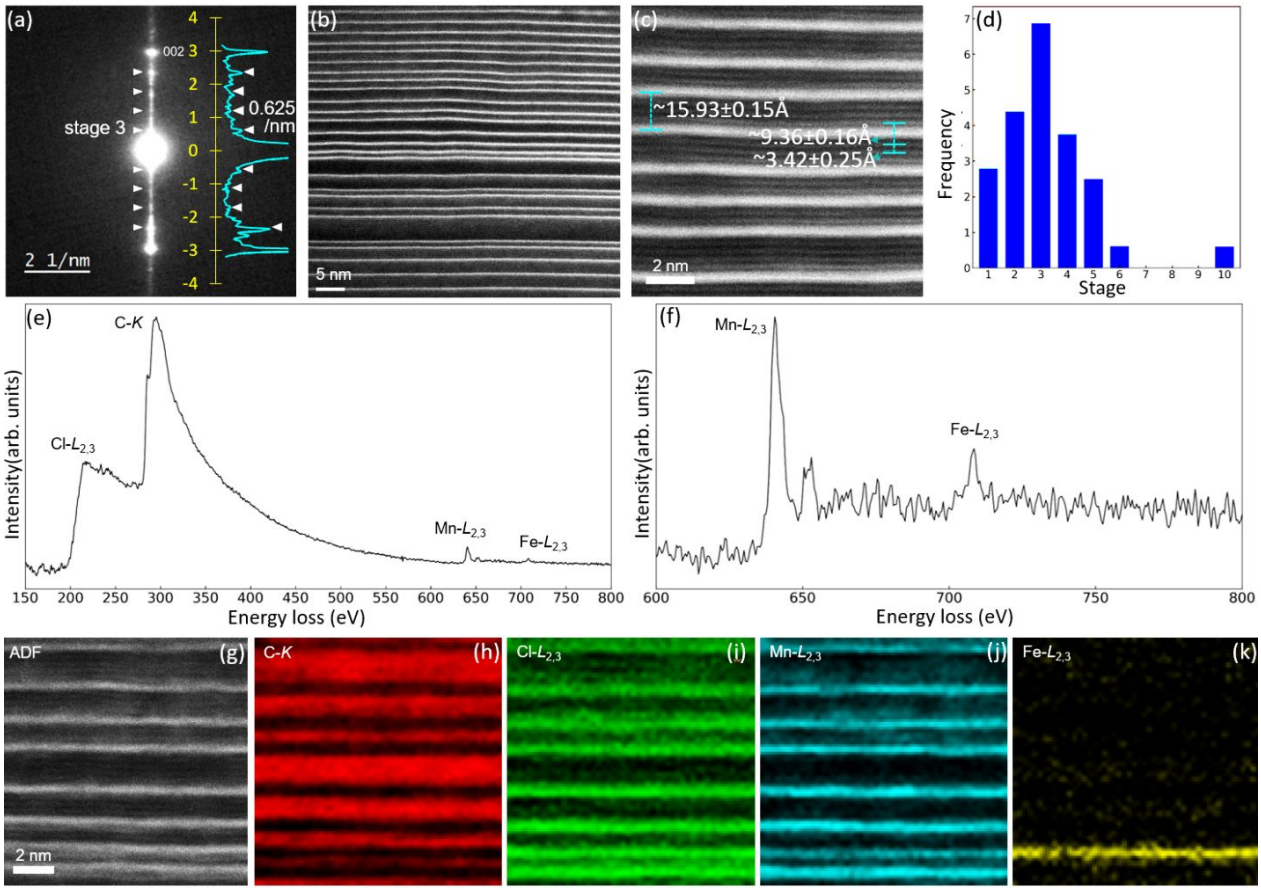

Figure 2: (a) SAED spots confirming the stage-3 lattice structure with the bright spots spaced ~0.34 nm apart, corresponding to the characteristic hexagonal 002 lattice-plane spacing of graphite. (b) ADF–STEM image of the GIC. The white horizontal lines and black regions represent intercalant atoms and graphite regions, respectively. (c) Magnified image showing the contrast profiles between different atoms that confirms parallel intercalation and staging. (d) Stage-distribution histogram analysis indicating the predominance of the stage-3 lattice structure. (e)–(f) EELS spectra of the GIC showing Cl-$L_{2,3}$, C-K, Mn-$L_{2,3}$, and Fe-$L_{2,3}$ edges, consistent with the observations of the ADF–STEM image shown in (a–b). (g–k) EELS elemental mapping (C: red, Cl: green, Mn: blue, Fe: yellow) based on the integrated intensities of Cl-$L_{2,3}$, C-K, Mn-$L_{2,3}$, and Fe-$L_{2,3}$ edges.

Furthermore, Mn and Cl were confirmed to concomitantly occupy similar positions along the in-plane and cross-plane directions, indicating their existence in the form of a stable compound (such as $MnCl_x$). The oxidation-state analysis of Mn (Supplementary Information, Section S3) indicated x = 2. According to the intensity ratio between Mn-L_3 and L_2 edges, it was confirmed that Mn oxidation state is +2, indicating the formation of stable $MnCl_2$. The Mn/Fe atomic-percentage ratio determined by EELS was 7.2, indicating the selective intercalation of Mn into the host graphite. In the Mn/Fe ratio of 7.2 estimated from local nanoscale-probing by EELS. Therefore, the elemental composition of the GIC sample was not just a surface or local phenomenon, but inherent to the material structure, independent of the scale of observation. This consistency across different scales of analysis validates the findings of this study and confirms the robustness and reliability of the analytical techniques used here. Inductively coupled plasma optical emission spectrometry (ICP–OES) was used to investigate the source of Mn in the co-GIC samples (Supplementary Information Section S2). The

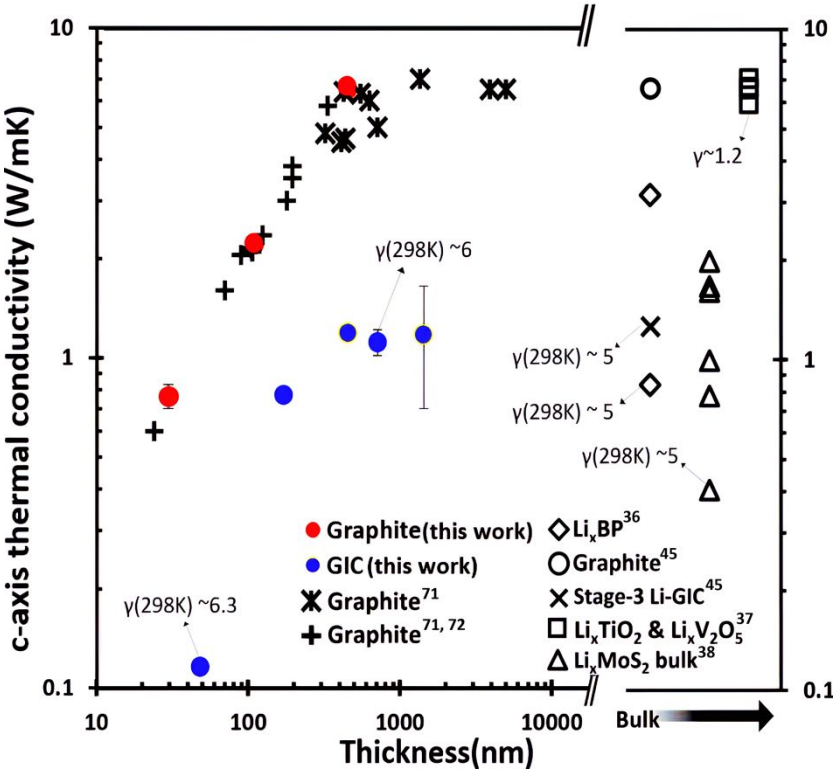

Figure 3: Thickness dependence of the c-axis thermal conductivity (κ_z) of graphite and its intercalated derivatives. The κ_z of the GICs are compared with those of Li-intercalated black phosphorous[36], TiO_2[37], V_2O_5[37], MoS_2[38] and graphite[45] in the literature. A good contrast is observed between the κ_z of their host material and intercalated system synthesized in this study. Here, γ indicates the reduction ratio, i.e., $\kappa_{pristine}/\kappa_{intercalated}$.

Figure 2k, Fe is predominantly at the bottom which can be speculated to stem from factors such as temperature gradient in intercalated layers and TEM induced electron beam damages [2, 43, 67-70], however limited TEM images prevent confirming this trend. A method to visualize and identify such distribution at both nanoscale and microscale is needed but currently unavailable. Scanning electron microscopy with energy dispersive X-Ray analysis (SEM–EDX) was used to confirm the consistent presence of $MnCl_2$ in an area wider than the STEM field of view. Prior to analysis, the surface of the GIC sample was cleaned by pure water, dried at 110 °C for 10 min, and subjected to ozone cleaning for 10 min to avoid Fe contamination owing to the adsorption of $FeCl_3$ powder. The SEM–EDX spatial scan of the GIC sample shown in Figure S5.2 confirms the presence of Mn in the sample and an Mn/Fe ratio of 7, indicating a homogenous spatial distribution of Mn and scattered spatial spread of Fe. Thus, compared with Fe, Mn is preferentially and uniformly dispersed throughout the material. Notably, the Mn/Fe ratio determined on a broader scale (spanning micrometers) was in close agreement with $FeCl_3$ powder was confirmed to contain a small amount of Mn with an Mn/Fe ratio of ~1/300. The significant difference (of nearly three orders of magnitude) between the Mn/Fe ratios of the powder and GIC samples indicates that Mn is preferentially intercalated within the vdW interlayers of graphite under the experimental conditions of this study. This phenomenon can be attributed to the temperature used for intercalation in this study (400 °C), which is significantly higher than the temperatures used in previous studies on the intercalation of GICs with $FeCl_3$ (300–350 °C). Although the co-intercalation of GICs with $MnCl_2$ and $FeCl_3$ was not an original aim of this study, the thermal conductivity tunability of the co-intercalated compound was extensively investigated. The cross-plane (c-axis) thermal conductivity (κ_z) of pristine graphite and co-GIC thin films were measured by time-domain thermoreflectance (TDTR)[59]. The room-temperature κ_z is shown as a function of the thin-film thickness in Figure 3. For the pristine graphite thin films, the measured magnitudes and trends are consistent with those reported by Zhang et al.[71] and Fu et al.[72]. Additionally, the measured κ_z of the thickest

pristine-graphite thin film lies within 6.3–7 $Wm^{-1}K^{-1}$, in good agreement with the literature value of 6.8 $Wm^{-1}K^{-1}$ [73]. Interestingly, intercalation caused a significant reduction in κ_z. On intercalation, the κ_z of three representative pristine-graphite thin films with thicknesses of 450, 110, and 30 nm reduced from 6.52, 2.21, and 0.76 $Wm^{-1}K^{-1}$ to 1.12, 0.77, and 0.12 $Wm^{-1}K^{-1}$, respectively, while their thicknesses increased to 710, 170, and 45 nm, respectively. A comparison of the κ_z values of the co-GICs with those of similar compounds in the literature, such as Li-intercalated black phosphorous[36], TiO_2[37], V_2O_5[37], MoS_2[38] and graphite[45], confirms the ability of the proposed method to tune the κ_z of the host material. The proposed method facilitates a significantly greater κ_z controllability (with a κ_z reduction ratio, defined as $\gamma = \kappa_{pristine}/\kappa_{intercalated}$, of ~6) than those reported previously.

Figure 3 shows the size effect in the system, which indicates that the thermal transport in the system becomes quasi-ballistic when the thickness of the sample becomes smaller than the p-MFP, and the $\boldsymbol{\kappa}_z$ is reduced owing to a thickness reduction due to boundary scattering. The reduction in $\boldsymbol{\kappa}_z$ starts at a thickness of ~400 nm, possibly because the longest MFP of phonons that contribute significantly to the $\boldsymbol{\kappa}_z$ of bulk graphite lies within 300–400 nm[71, 74]. A steep reduction in $\boldsymbol{\kappa}_z$ is observed on reducing the thickness of co-GIC samples below ~400 nm, possibly because the effective phonon MFP is shorter than the sample thickness in these cases. Notably, despite the significant size effect, the γ of the system remains high (~6) consistently, even for the thinnest sample, indicating that the intercalation effect is extremely effective in reducing the $\boldsymbol{\kappa}_z$ of the system.

Figure 4 shows the temperature dependence of the $\boldsymbol{\kappa}_z$ of pristine graphite and co-GIC samples within 78–298 K. The experimentally observed temperature dependence of the pristine-graphite thin film is in good agreement with previous reports[71], while that of the 450-nm-thick graphite film is consistent with those of both 428- and 627-nm-thick graphite films reported in the literature, possibly because these systems are free from the size effect owing to a greater thickness than the p-MFP. On decreasing the temperature below room temperature, the $\boldsymbol{\kappa}_z$ of the 450-nm-thick graphite film first increases, peaks at ~125 K, and finally decreases. The appearance of the peak can be attributed to a balance between the two effects that reduce the $\boldsymbol{\kappa}_z$ of the system, i.e., the quantum effect on the heat capacity and intrinsic phonon-phonon scattering; the former predominates at low temperatures and gradually reduces on increasing the temperature, while the latter predominates at high temperatures and gradually increases on enhancing the temperature.

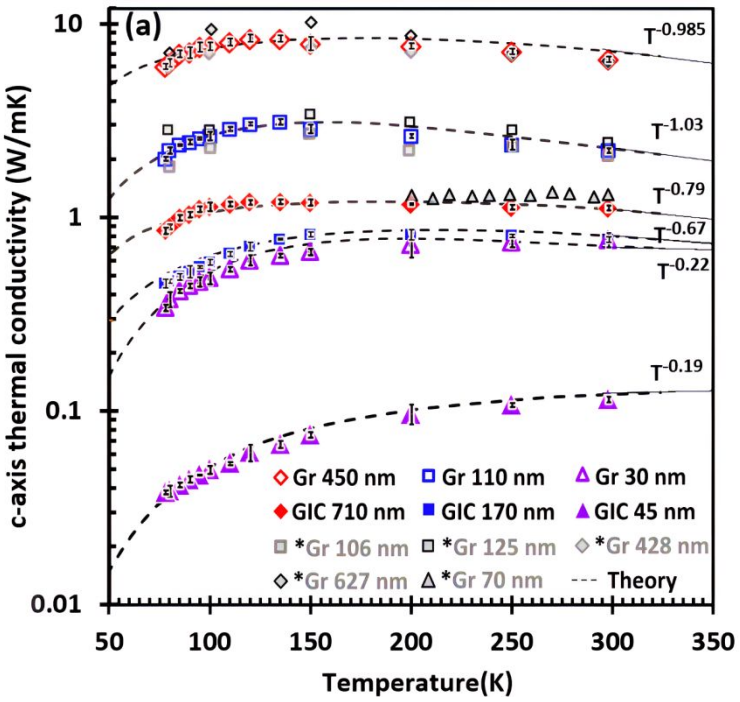

Figure 4: Measured data fitted to the Debye–Callaway model to investigate the temperature dependence of κ_z of graphite and the GIC counterparts in the log-scale. The data from the literature[62-63] and are marked with a superscript asterisk (*) in the legend. The temperature exponent follows the power scaling law at high temperatures.

At temperatures >125 K, the 450- and 110-nm-thick films follow the characteristic T^{-1} power law that is attributed solely to Umklapp scattering; the 30-nm-thick film shows a relatively weaker dependence on the law. Contrarily, at high temperatures, the temperature dependence of the co-GICs, regardless of their thickness, deviates from the T^{-1} law and the curve gradually becomes flatter without any noticeable peak.

To study the underlying mechanism of the observed tunability of $\boldsymbol{\kappa}_z$ upon intercalation, the measured temperature-dependent $\boldsymbol{\kappa}_z$ was fit to the Debye–Callaway model (Eq. (7))[56], an empirical model based on phonon kinetics (See Materials and Methods and

Supplementary Information Section S6) that considers the frequency and temperature dependence of phonon-scattering phenomena. Key phonon-scattering phenomena, namely, Umklapp scattering, impurity scattering, boundary scattering from the edges of sample before and after intercalation, and intercalation scattering originating from the foreign-atom guest layers with the scattering rates τ_U^{-1}, τ_{Imp}^{-1}, τ_B^{-1}, and τ_{Intc}^{-1}, respectively, were considered in this study. As τ_B^{-1} is a function of the physical dimensions of the sample, the way to model the intercalation scattering is not evident, it was implemented it in the same fashion as boundary scattering, giving a fixed length scale (λ_{Intc}) for scattering (See Materials and Methods). The c-axis phonon group velocity (v) in Eq. (7) was measured using picosecond acoustic echo signals with TDTR[60] (See Supplementary Information Section S1.2); v underwent significant modulation on intercalation. On intercalation, the v of pristine-graphite thin film with a thickness of 30 nm decreased from 4050 to ~2835 m/s,

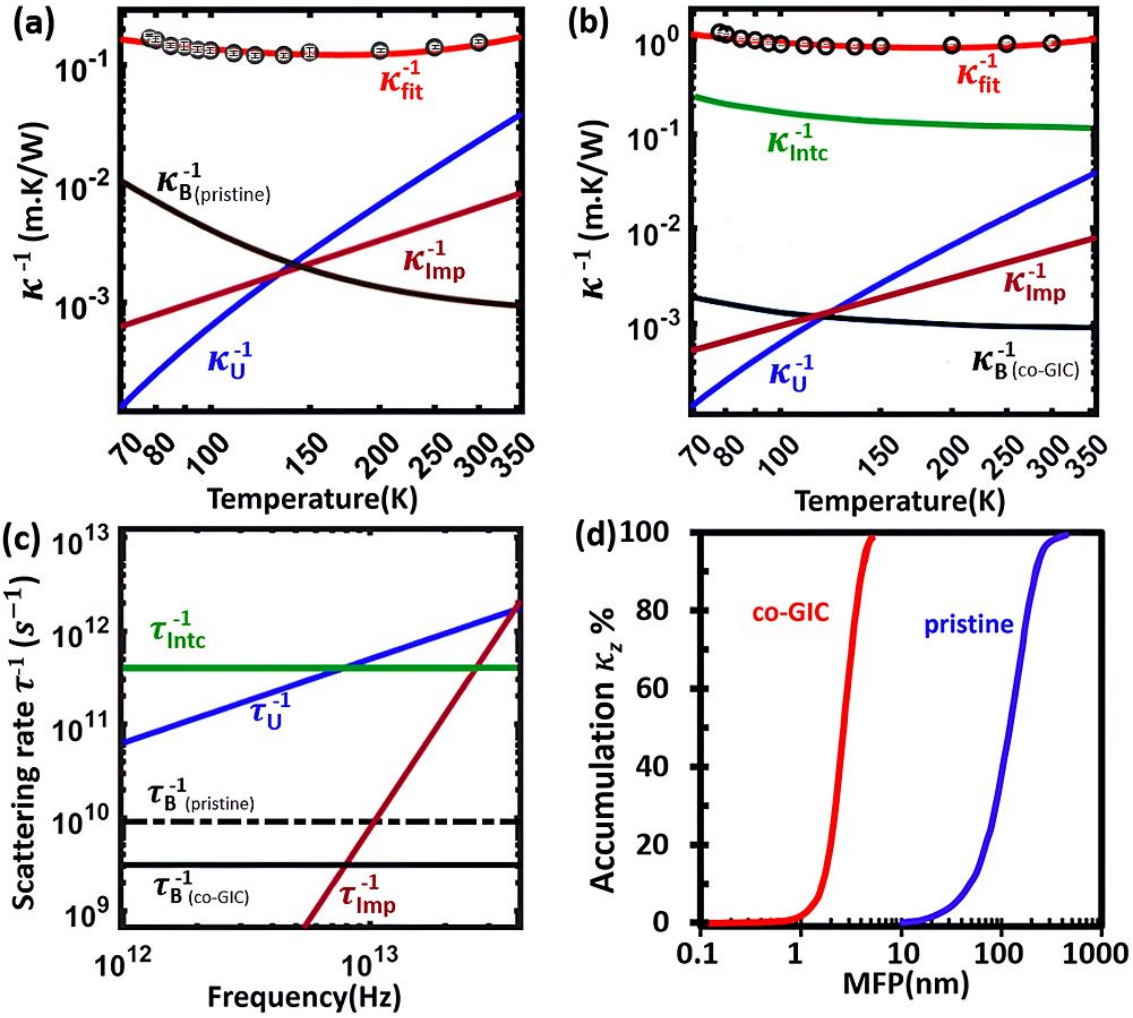

Figure 5: Thermal resistivity contributions from various phonon scattering mechanisms for a 450-nm-thick pristine graphite film (a) before intercalation and (b) after intercalation (for its co-GIC counterpart with a thickness of 710 nm). (c) Room-temperature phonon-scattering-rate contributions of various scattering mechanisms vs. the frequency of phonon vibrations before and after intercalation. (d) The accumulated thermal conductivity dependence on the pMFP indicates a significant reduction in the MFP upon intercalation.

the actual thickness of the sample before and after intercalation was used as the scattering length. The values of τ_U^{-1} and τ_{Imp}^{-1} were estimated by fitting the measured temperature-dependent thermal conductivity before intercalation to the model, assuming the parameters to remain unchanged on intercalation. Parameters have been tubulated and presented in Supplementary Information S6.1. Intercalation scattering originating from foreign-atom guest layers is only applicable on intercalation; therefore, τ_{Intc}^{-1} was determined by fitting the experimentally measured temperature-dependent thermal conductivity of the co-GIC samples to the model. Here, while forming a co-GIC with a thickness of 45 nm, possibly owing to the softening of the harmonic force constant of the system. This can be elaborated by calculating and the in van der Waals binding energy from Lennard-Jones potential parameters, where effective atom pair interaction between carbon and $MnCl_2$ is weaker than that between carbons. (See Supplementary Information Section S6.2). The fitted thermal-conductivity models for pristine graphite and co-GIC are shown in Figure 4 by dashed lines. The models accurately indicate the temperature dependence and intercalation-induced reduction in κ_z in all the samples. Notably, λ_{Intc} is the only fitting parameter used

for co-GIC; the excellent goodness of fit confirms intercalation scattering via boundary scattering. This can be understood by considering the intercalant layer as a grain boundary of graphite. Additionally, the low value of λ_{Intc} (~3 nm) indicates that intercalation enables graphite to exhibit an extremely small scattering length scale on graphite, which is difficult to realize using other nanostructuring schemes. Notably, the scattering length (3 nm) is still somewhat larger than the distance between stage-*3* intercalation layers (~1 nm), possibly owing to various factors such as nonzero transmission at the intercalant layer and uncertainty in the completion of intercalation. Therefore, it should be possible to reduce the thermal conductivity of the system further. Note that the extracted length scale is an effective value, approximately projecting the intercalation effect onto the boundary-scattering type scenario.

The contributions of different scattering mechanisms to the thermal conductivity of the system are shown in Figure 5(a), (b), which indicates competition among Umklapp scattering, impurity scattering, boundary scattering, and intercalation-induced scattering in the system before and after intercalation in terms of their thermal-resistivity contributions ($\boldsymbol{\kappa_U^{-1}}$, $\boldsymbol{\kappa_{Imp}^{-1}}$, $\boldsymbol{\kappa_B^{-1}}$, and $\boldsymbol{\kappa_{Intc}^{-1}}$, respectively). Intercalation scattering significantly influenced the total lattice thermal resistivity (by nearly an order of magnitude) of the system over the entire experimental temperature range. As shown in Figure 5(a), boundary scattering predominantly influences the thermal resistivity ($\boldsymbol{\kappa_z^{-1}}$) of the 450-nm-thick unintercalated graphite film up to a temperature of ~125 K; beyond this temperature, Umklapp scattering predominates, significantly limiting thermal transport. After intercalation, as shown in Figure 5(b), intercalation scattering predominantly influences thermal transport, surpassing the contribution of Umklapp scattering across the entire experimental temperature range. The room-temperature scattering rates for different scattering mechanisms, calculated using Eq. (1)–(6) (See Materials and Methods), are shown in Figure 5(c). After intercalation, the intercalation scattering rate becomes 50 times that of the boundary scattering rate of a pristine-graphite sample within the same frequency range (0–3 THz); the phenomenon of boundary scattering sustains cross-plane conduction in graphite. Notably, the predominance of intercalation scattering explains the reduction in the temperature dependence of $\boldsymbol{\kappa_z}$ on intercalation. The theoretical fit results of the accumulated thermal conductivity with respect to the p-MFP shown in Figure 5(d) indicate that the characteristic length of $\boldsymbol{\kappa_z}$ reduces significantly on intercalation (from several hundred nanometers to a few nanometers), validating the conclusions drawn from the experimental results (See Supplementary Information Section S6 for more details).

Conclusions

In summary, this study reports the effective tuning of $\boldsymbol{\kappa_z}$ in graphite films with different thicknesses upon co-intercalation with $MnCl_2$ and $FeCl_3$ as the major and minor components, respectively, thus forming a co-GIC. These samples were synthesized by physical vapor deposition using nearly pure $FeCl_3$ powder. Under specific synthesis conditions, a trace amount of Mn from the starting material was selectively intercalated into graphite, resulting in a co-GIC with an Mn/Fe ratio of ~7. The thickness and temperature dependences of the $\boldsymbol{\kappa_z}$ of the samples were measured by TDTR. The results indicated that the $\boldsymbol{\kappa_z}$ of the samples were effectively controlled by intercalation with a reduction ratio of up to 6. The large reduction ratio was sustained, even for samples with thicknesses less than 100 nm, confirming the robustness of the intercalation-based strategy to control $\boldsymbol{\kappa_z}$, despite enhanced boundary scattering. The temperature dependences of $\boldsymbol{\kappa_z}$ were fitted to a semi-empirical Debye-Callaway model and the relative contributions of various scattering mechanisms were quantified. Upon intercalation, strong intercalation scattering was operative in the system, which predominantly influenced and limited the $\boldsymbol{\kappa_z}$. This phenomenon was attributed to a ~45-fold increment in the room-temperature intercalation scattering rate. Additionally, on intercalation, owing to the weakening of interlayer interactions in the graphite system, the c-axis phonon-propagation velocity reduced by ~30% (from 4050 to 2835 m/s) due to changes in the c-axis lattice constant caused by the softening of the interlayer force constant at every intercalant repeat distance. The combination of these two effects resulted in a significant reduction in the p-MFP of graphite (by two orders of magnitude) upon intercalation. Thus, this work provides insight into the underlying phonon-scattering mechanism that enables the effective modulation of the $\boldsymbol{\kappa_z}$ of graphite on intercalation. Moreover, the results of this study are a proof-of-concept for the fabrication of novel materials with excellent cross-plane thermal-conductivity tunability through intercalation. Therefore, this study could guide the future development of materials with unique thermal properties.

Acknowledgments

The authors thank Yuki Kanazawa, Hideaki Tanaka, and Sumire Miyakoshi at Waseda University for their supports with intercalation treatments and ICP-OES measurements. This study was financially supported by JST CREST (Grant No. JPMJCR21O2) and a Grant-in-Aid for Scientific Research (KAKENHI: 22H04950). This study was partially supported by the "Advanced Research Infrastructure for Materials and Nanotechnology in Japan (ARIM)" of the Ministry of Education, Culture, Sports, Science and Technology (MEXT).

References

(1) Chen, G. Non-Fourier phonon heat conduction at the microscale and nanoscale. *Nature Reviews Physics* **2021**, *3* (8), 555-569.
(2) Toyoura, K.; Koyama, Y.; Kuwabara, A.; Oba, F.; Tanaka, I. First-principles approach to chemical diffusion of lithium atoms in a graphite intercalation compound. *Physical Review B—Condensed Matter and Materials Physics* **2008**, *78* (21), 214303.
(3) Liu, S.; Xu, X.; Xie, R.; Zhang, G.; Li, B. Anomalous heat conduction and anomalous diffusion in low dimensional nanoscale systems. *The European Physical Journal B* **2012**, *85*, 1-20.
(4) Basile, G.; Bernardin, C.; Olla, S. Momentum conserving model with anomalous thermal conductivity in low dimensional systems. *Physical review letters* **2006**, *96* (20), 204303.
(5) Luckyanova, M. N.; Garg, J.; Esfarjani, K.; Jandl, A.; Bulsara, M. T.; Schmidt, A. J.; Minnich, A. J.; Chen, S.; Dresselhaus, M. S.; Ren, Z. Coherent phonon heat conduction in superlattices. *Science* **2012**, *338* (6109), 936-939.

(6) Cepellotti, A.; Fugallo, G.; Paulatto, L.; Lazzeri, M.; Mauri, F.; Marzari, N. Phonon hydrodynamics in two-dimensional materials. *Nature communications* **2015**, *6* (1), 6400.
(7) Zhang, H.; Hua, C.; Ding, D.; Minnich, A. J. Length dependent thermal conductivity measurements yield phonon mean free path spectra in nanostructures. *Scientific Reports* **2015**, *5* (1), 9121.
(8) Zeng, L.; Collins, K. C.; Hu, Y.; Luckyanova, M. N.; Maznev, A. A.; Huberman, S.; Chiloyan, V.; Zhou, J.; Huang, X.; Nelson, K. A. Measuring phonon mean free path distributions by probing quasiballistic phonon transport in grating nanostructures. *Scientific reports* **2015**, *5* (1), 17131.
(9) Saha, B.; Koh, Y. R.; Comparan, J.; Sadasivam, S.; Schroeder, J. L.; Garbrecht, M.; Mohammed, A.; Birch, J.; Fisher, T.; Shakouri, A. Cross-plane thermal conductivity of (Ti, W) N/(Al, Sc) N metal/semiconductor superlattices. *Physical Review B* **2016**, *93* (4), 045311.
(10) Maldovan, M. Phonon wave interference and thermal bandgap materials. *Nature materials* **2015**, *14* (7), 667-674.
(11) Hu, R.; Iwamoto, S.; Feng, L.; Ju, S.; Hu, S.; Ohnishi, M.; Nagai, N.; Hirakawa, K.; Shiomi, J. Machine-learning-optimized aperiodic superlattice minimizes coherent phonon heat conduction. *Physical Review X* **2020**, *10* (2), 021050.
(12) Ju, S.; Shiga, T.; Feng, L.; Hou, Z.; Tsuda, K.; Shiomi, J. Designing nanostructures for phonon transport via Bayesian optimization. *Physical Review X* **2017**, *7* (2), 021024.
(13) Dresselhaus, M. S. Intercalation in layered materials. *MRS Bulletin* **1987**, *12*, 24-28.
(14) Kambe, N.; Dresselhaus, G.; Dresselhaus, M. Electron diffraction from superlattices in graphite-rubidium intercalation compounds. *Physical Review B* **1980**, *21* (8), 3491.
(15) Hwang, D.; Parker, N.; Utlaut, M.; Crewe, A. Observation of nonhexagonal superlattices in high-stage cesium intercalated graphite. *Physical Review B* **1983**, *27* (2), 1458.
(16) Stankovich, S.; Dikin, D. A.; Dommett, G. H.; Kohlhaas, K. M.; Zimney, E. J.; Stach, E. A.; Piner, R. D.; Nguyen, S. T.; Ruoff, R. S. Graphene-based composite materials. *nature* **2006**, *442* (7100), 282-286.
(17) Shahil, K. M.; Balandin, A. A. Thermal properties of graphene and multilayer graphene: Applications in thermal interface materials. *Solid state communications* **2012**, *152* (15), 1331-1340.
(18) Sang, M.; Shin, J.; Kim, K.; Yu, K. J. Electronic and thermal properties of graphene and recent advances in graphene based electronics applications. *Nanomaterials* **2019**, *9* (3), 374.
(19) Gong, C.; Zhang, Y.; Chen, W.; Chu, J.; Lei, T.; Pu, J.; Dai, L.; Wu, C.; Cheng, Y.; Zhai, T. Electronic and optoelectronic applications based on 2D novel anisotropic transition metal dichalcogenides. *Advanced Science* **2017**, *4* (12), 1700231.
(20) Huang, H.; Zha, J.; Li, S.; Tan, C. Two-dimensional alloyed transition metal dichalcogenide nanosheets: Synthesis and applications. *Chinese Chemical Letters* **2022**, *33* (1), 163-176.
(21) Shahzad, F.; Iqbal, A.; Kim, H.; Koo, C. M. 2D transition metal carbides (MXenes): applications as an electrically conducting material. *Advanced Materials* **2020**, *32* (51), 2002159.
(22) Fu, B.; Sun, J.; Wang, C.; Shang, C.; Xu, L.; Li, J.; Zhang, H. MXenes: Synthesis, optical properties, and applications in ultrafast photonics. *Small* **2021**, *17* (11), 2006054.
(23) Zhang, C. J.; Nicolosi, V. Graphene and MXene-based transparent conductive electrodes and supercapacitors. *Energy Storage Materials* **2019**, *16*, 102-125.
(24) Zheng, Z.; Cox, M.; Li, B. Surface modification of hexagonal boron nitride nanomaterials: a review. *Journal of Materials Science* **2018**, *53*, 66-99.
(25) Meziani, M. J.; Song, W. L.; Wang, P.; Lu, F.; Hou, Z.; Anderson, A.; Maimaiti, H.; Sun, Y. P. Boron nitride nanomaterials for thermal management applications. *ChemPhysChem* **2015**, *16* (7), 1339-1346.
(26) Xie, H.; Ouyang, T.; Germaneau, É.; Qin, G.; Hu, M.; Bao, H. Large tunability of lattice thermal conductivity of monolayer silicene via mechanical strain. *Physical Review B* **2016**, *93* (7), 075404.
(27) Shan, G.; Tan, H.; Ma, R.; Zhao, H. B.; Huang, W. Recent progress in emergent two-dimensional silicene. *Nanoscale* **2023**.
(28) Chegel, R.; Behzad, S. Tunable electronic, optical, and thermal properties of two-dimensional germanene via an external electric field. *Scientific Reports* **2020**, *10* (1), 704.
(29) Kou, L.; Chen, C.; Smith, S. C. Phosphorene: fabrication, properties, and applications. *The journal of physical chemistry letters* **2015**, *6* (14), 2794-2805.
(30) Fei, R.; Faghaninia, A.; Soklaski, R.; Yan, J.-A.; Lo, C.; Yang, L. Enhanced thermoelectric efficiency via orthogonal electrical and thermal conductances in phosphorene. *Nano letters* **2014**, *14* (11), 6393-6399.
(31) Li, H.; Ying, H.; Chen, X.; Nika, D. L.; Cocemasov, A. I.; Cai, W.; Balandin, A. A.; Chen, S. Thermal conductivity of twisted bilayer graphene. *Nanoscale* **2014**, *6* (22), 13402-13408.
(32) Ren, W.; Ouyang, Y.; Jiang, P.; Yu, C.; He, J.; Chen, J. The impact of interlayer rotation on thermal transport across graphene/hexagonal boron nitride van der Waals heterostructure. *Nano Letters* **2021**, *21* (6), 2634-2641.
(33) Hu, S.; Ju, S.; Shao, C.; Guo, J.; Xu, B.; Ohnishi, M.; Shiomi, J. Ultimate impedance of coherent heat conduction in van der Waals graphene-MoS2 heterostructures. *Materials Today Physics* **2021**, *16*, 100324.
(34) Gao, Y.; Liu, Q.; Xu, B. Lattice mismatch dominant yet mechanically tunable thermal conductivity in bilayer heterostructures. *ACS nano* **2016**, *10* (5), 5431-5439.
(35) Abramson, A. R.; Tien, C.-L.; Majumdar, A. Interface and strain effects on the thermal conductivity of heterostructures: A molecular dynamics study. *J. Heat Transfer* **2002**, *124* (5), 963-970.
(36) Kang, J. S.; Ke, M.; Hu, Y. Ionic intercalation in two-dimensional van der Waals materials: in situ characterization and electrochemical control of the anisotropic thermal conductivity of black phosphorus. *Nano Letters* **2017**, *17* (3), 1431-1438.
(37) Shin, J.; Kim, S.; Park, H.; Jang, H. W.; Cahill, D. G.; Braun, P. V. Thermal conductivity of intercalation, conversion, and alloying lithium-ion battery electrode materials as function of their state of charge. *Current Opinion in Solid State and Materials Science* **2022**, *26* (2), 100980.
(38) Zhu, G.; Liu, J.; Zheng, Q.; Zhang, R.; Li, D.; Banerjee, D.; Cahill, D. G. Tuning thermal conductivity in molybdenum disulfide by electrochemical intercalation. *Nature communications* **2016**, *7* (1), 13211.
(39) Lu, Q.; Huberman, S.; Zhang, H.; Song, Q.; Wang, J.; Vardar, G.; Hunt, A.; Waluyo, I.; Chen, G.; Yildiz, B. Bi-directional tuning of thermal transport in SrCoO x with electrochemically induced phase transitions. *Nature Materials* **2020**, *19* (6), 655-662.
(40) Wan, C.; Kodama, Y.; Kondo, M.; Sasai, R.; Qian, X.; Gu, X.; Koga, K.; Yabuki, K.; Yang, R.; Koumoto, K. Dielectric mismatch mediates carrier mobility in organic-intercalated layered TiS2. *Nano letters* **2015**, *15* (10), 6302-6308.
(41) Wan, C.; Gu, X.; Dang, F.; Itoh, T.; Wang, Y.; Sasaki, H.; Kondo, M.; Koga, K.; Yabuki, K.; Snyder, G. J. Flexible n-type thermoelectric materials by organic intercalation of layered transition metal dichalcogenide TiS 2. *Nature materials* **2015**, *14* (6), 622-627.

(42) Xiong, Y.; Lai, N.-C.; Lu, Y.-C.; Xu, D. Tuning thermal conductivity of bismuth selenide nanoribbons by reversible copper intercalation. *International Journal of Heat and Mass Transfer* **2020**, *159*, 120077.
(43) Dresselhaus, M.; Dresselhaus, G. Intercalation compounds of graphite. *Advances in Physics* **1981**, *30* (2), 139-326.
(44) Leung, S.; Dresselhaus, M.; Dresselhaus, G. Infrared and Raman spectroscopy of graphite intercalation compounds. *Physica B+ C* **1981**, *105* (1-3), 375-380.
(45) Qian, X.; Gu, X.; Dresselhaus, M. S.; Yang, R. Anisotropic tuning of graphite thermal conductivity by lithium intercalation. *The journal of physical chemistry letters* **2016**, *7* (22), 4744-4750.
(46) Solin, S.; Zabel, H. The physics of ternary graphite intercalation compounds. *Advances in Physics* **1988**, *37* (2), 87-254.
(47) Shornikova, O.; Dunaev, A.; Maksimova, N.; Avdeev, V. Synthesis and properties of ternary GIC with iron or copper chlorides. *Journal of Physics and Chemistry of Solids* **2006**, *67* (5-6), 1193-1197.
(48) Scharff, P.; Stumpp, E. Electrochemical study of the intercalation reactions of perchloric and nitric acid. *Berichte der Bunsengesellschaft für physikalische Chemie* **1991**, *95* (1), 58-61.
(49) Scharff, P.; Stumpp, E.; Ehrhardt, C. Electrochemical preparation and characterization of novel graphite bi-intercalation compounds. *Synthetic Metals* **1988**, *23* (1-4), 415-420.
(50) Tatsumi, K.; Shioyama, H.; Souma, I.; Fujii, R. In situ XRD observations of the formation of the graphite bi-intercalation compound with BiCl3 and HClO4. *Carbon (New York, NY)* **1990**, *28* (4), 595-597.
(51) Inagaki, M.; Ohira, M. Intercalation of AlCl3 into FeCl3-graphite intercalation compounds and occurrence of BI-intercalation. *Carbon* **1993**, *31* (5), 777-781.
(52) Abe, T.; Mizutani, Y.; Asano, M.; Harada, T. Preparation of stages 2–4 ternary AlCl3–FeCl3-graphite intercalation compounds. *Journal of materials research* **1995**, *10* (5), 1196-1199.
(53) Inagaki, M.; Mitsuhashi, T.; Soneda, Y. Intercalation into graphite of metal chlorides from organic solutions. *JOURNAL DE CHIMIE PHYSIQUE ET DE PHYSICO-CHIMIE BIOLOGIQUE* **1987**, *84* (11-12), 1439-1442.
(54) Tanaike, O.; Hoshino, Y.; Inagaki, M. Different reactivity of carbon materials for intercalation of iron chloride in its nitromethane solution. *Synthetic metals* **1999**, *99* (2), 105-110.
(55) Kang, F.; Leng, Y.; Zhang, T.-Y.; Li, B. Electrochemical synthesis and characterization of ferric chloride-graphite intercalation compounds in aqueous solution. *Carbon* **1998**, *36* (4), 383-390.
(56) Callaway, J. Model for lattice thermal conductivity at low temperatures. *Physical Review* **1959**, *113* (4), 1046.
(57) Geim, A. K.; Kim, P. Carbon wonderland. *Scientific American* **2008**, *298* (4), 90-97.
(58) Ishikawa, R.; Lupini, A. R.; Findlay, S. D.; Pennycook, S. J. Quantitative annular dark field electron microscopy using single electron signals. *Microscopy and Microanalysis* **2014**, *20* (1), 99-110.
(59) Cahill, D. G. Analysis of heat flow in layered structures for time-domain thermoreflectance. *Review of scientific instruments* **2004**, *75* (12), 5119-5122.
(60) Zheng, Q.; Braun, P. V.; Cahill, D. G. Thermal conductivity of graphite thin films grown by low temperature chemical vapor deposition on Ni (111). *Advanced Materials Interfaces* **2016**, *3* (16), 1600234.
(61) Iyo, A.; Ogino, H.; Ishida, S.; Eisaki, H. Dramatically Accelerated Formation of Graphite Intercalation Compounds Catalyzed by Sodium. *Advanced Materials* **2023**, *35* (15), 2209964.
(62) Enoki, T.; Suzuki, M.; Endo, M. *Graphite intercalation compounds and applications*; Oxford University Press, 2003.
(63) Chacón‐Torres, J. C.; Wirtz, L.; Pichler, T. Raman spectroscopy of graphite intercalation compounds: Charge transfer, strain, and electron–phonon coupling in graphene layers. *physica status solidi (b)* **2014**, *251* (12), 2337-2355.
(64) Walter, J.; Shioyama, H.; Sawada, Y.; Hara, S. Electron diffraction and scanning tunneling microscope studies of TaCl5-graphite intercalation compounds. *Carbon* **1998**, *36* (9), 1277-1284.
(65) Wang, G.; Yang, J.; Park, J.; Gou, X.; Wang, B.; Liu, H.; Yao, J. Facile synthesis and characterization of graphene nanosheets. *The Journal of Physical Chemistry C* **2008**, *112* (22), 8192-8195.
(66) Ishikawa, R.; Lugg, N. R.; Inoue, K.; Sawada, H.; Taniguchi, T.; Shibata, N.; Ikuhara, Y. Interfacial atomic structure of twisted few-layer graphene. *Scientific reports* **2016**, *6* (1), 21273.
(67) Dresselhaus, G.; Dresselhaus, M. S.; Saito, R. *Physical properties of carbon nanotubes*; World scientific, 1998.
(68) Van der Ven, A.; Bhattacharya, J.; Belak, A. A. Understanding Li diffusion in Li-intercalation compounds. *Accounts of chemical research* **2013**, *46* (5), 1216-1225.
(69) Dedkov, Y.; Voloshina, E. Spectroscopic and DFT studies of graphene intercalation systems on metals. *Journal of Electron Spectroscopy and Related Phenomena* **2017**, *219*, 77-85.
(70) Salamanca-Riba, L.; Roth, G.; Gibson, J.; Kortan, A.; Dresselhaus, G.; Birgeneau, R. Electron-beam-induced damage and structure of SbCl 5-graphite intercalation compounds. *Physical Review B* **1986**, *33* (4), 2738.
(71) Zhang, H.; Chen, X.; Jho, Y.-D.; Minnich, A. J. Temperature-dependent mean free path spectra of thermal phonons along the c-axis of graphite. *Nano letters* **2016**, *16* (3), 1643-1649.
(72) Fu, Q.; Yang, J.; Chen, Y.; Li, D.; Xu, D. Experimental evidence of very long intrinsic phonon mean free path along the c-axis of graphite. *Applied Physics Letters* **2015**, *106* (3).
(73) Taylor, R. The thermal conductivity of pyrolytic graphite. *Philosophical Magazine* **1966**, *13* (121), 157-166.
(74) Yang, J.; Shen, M.; Yang, Y.; Evans, W. J.; Wei, Z.; Chen, W.; Zinn, A. A.; Chen, Y.; Prasher, R.; Xu, T. T. Phonon transport through point contacts between graphitic nanomaterials. *Physical Review Letters* **2014**, *112* (20), 205901.

Data availability statements:

The data supporting this article have been included as part of the Supplementary Information.